Shape-controlled synthesis of Cobalt particles by a surfactant-free solvothermal method and their catalytic application on the thermal decomposition of ammonium perchlorate

Dong Yan, Haiyan Zhao*, Yue Liu, Xin Wu, Jiayun Pei

Department of Mechanical Engineering, Tsinghua University, Beijing 100084, P. R. China and State Key Laboratory of Tribology, Tsinghua University, Beijing 100084, P. R. China

E-mail: hyzhao@tsinghua.edu.cn

Abstract

Sub-micro Co particles with different morphologies were successfully synthesized by a simple solvothermal and surfactant-free approach. Transmission electron microscope (TEM) and scanning electron microscope (SEM) images revealed that the average size was approximately 2 μm and microstructure of as-synthesize particles could be regulated by the contents and ratio of Co^{2+}/NaOH. The phase structure and composition for as-synthesized samples were characterized by X-ray diffraction (XRD), X-ray photoemission spectroscopy (XPS) and Raman spectrometer. Results indicated that the as-synthesized Co particles were covered with a thin layer of CoO. Based on the time-dependent experiments, the growth mechanism of three kinds of typical structures and morphologies were proposed. The magnetic hysteresis loops showed ferromagnetic characteristics and the best saturation magnetization (*Ms*) and coercivity (*Hc*) were 162.5 emu/g and 104.3 Oe, respectively. Moreover, the exothermic peak of ammonium perchlorate thermal decomposition shifted towards the lower temperatures by 93°C through adding 4% Co particles, indicating Co particles exhibited good catalytic effect for potential applications.

Introduction

As a typical metallic material, cobalt (Co) possesses excellent magnetic, electrical and catalytic properties, which are of scientific and technological interests in different fields.[1] High saturation magnetization and coercivity make Co become the preferred structure for high density information storage and permanent magnet applications.[2] Meantime, Cobalt particles also have an intrinsic advantage in biomedical fields, eg.

drug delivery and magnetic resonance imaging.[3, 4]

Ammonium perchlorate (NH_4ClO_4 or AP) is the main oxidizer of composite solid rocket propellants.[5] The performance of composite solid rocket propellants strongly depends on the thermal decomposition of AP, which is significantly influenced by catalysts or solid additives.[6] The lower decomposition temperature and more exothermic heat are important for the utilization of AP. Recently, there are some researches reported the effect of catalytic activity of different morphologies of cobalt oxide (eg. Co_3O_4 nanoparticles) on the decomposition of AP.[7, 8] However, the catalytic activity of cobalt was reported more sensitive and effective than that of cobalt oxide.[9]

The excellent catalytic properties of Co particles are closely related with their crystal phases and morphologies. Therefore, developing shape-controlled synthesis of cobalt particles has attracted great research interest. So far, various Co structures such nanosheets, spheres, snowflake or cauliflower-like particles, leaf-shaped flakes, microchains have been synthesized by numerous methods.[10-14] Among these approaches, a facile hydrothermal/solvothermal route is an ambitious method due to its convenient and inexpensive merit. However, the surfactants such as poly (vinyl pyrrolidone) (PVP),[14, 15] oleic acid[16] and sodium dodecyl benzenesulfonate (SDBS)[17] which are always indispensable in hydrothermal/solvothermal route, would adsorb onto the surface of produces and are difficult to wash off. Thus, it is of great significance to develop a surfactant-free and green synthesis route to synthesize shape-controlled cobalt materials.

In current work, a simple solvothermal and surfactant-free approach was utilized to synthesize cobalt particles with controlled morphology. Using ethylene glycol (EG) as the reaction solution, the molar ratios of Co^{2+}/NaOH have been adjusted to regulate the morphology and size of Co sub-micro particles. By sampling at different reaction times, the possible formation mechanism was also put forward. To study their potential applications, the as-synthesized Co particles with different morphologies had been applied in the thermal decomposition of AP, exhibiting excellent catalytic performance.

Experimental

Magnetic cobalt particles were synthesized by $CoCl_2 \cdot 6H_2O$ and NaOH in ethylene glycol (EG). In typical procedure, 4 mmol $CoCl_2 \cdot 6H_2O$ and 15 mmol NaOH were separately dissolved into 20 mL EG under magnetic stirring, then two solutions were mixed together at room temperature and stirred for 30 min. The mixture was transferred to Teflon-lined stainless steel autoclave with a capacity of 50 mL, sealed and maintained at 200 °C for 10 h. After cooling to room temperature naturally, the precipitate was washed with ethanol and water for several times and then dried at 60 °C overnight. Meanwhile, different molar ratios of Co^{2+}/NaOH were investigated with the details shown in Table 1.

The morphology and size of the samples were observed by using scanning electron microscope (SEM, LEO-1530, Oberkochen, Germany) and transmission electron microscopy (TEM). The crystal structure of the sample was determined by X-ray diffraction (XRD) on a D8/ADVANCE diffractometer by using Cu-Kα radiation (λ=1.5418Å). X-ray photoemission spectroscopy (XPS) measurements were performed by using a spectrometer with Al-Kα radiation as the excitation source. Raman scattering was excited using the 633 nm radiation from He-Ne laser and was collected by a micro-Raman spectrometer (LabRAM, HR800) in the 100-1000 cm^{-1} range at room temperature. The magnetic properties were measured with a BHV-50HTI vibrating sample magnetometer (VSM). Differential scanning calorimeter (DSC) and thermogravimetric analysis (TGA) were using thermal analyzer with a heating rate of 10 °C min^{-1} in Ar atmosphere over the temperature range of 50–500 °C . The mass percentage of Co particles to AP in the mixture was 4%.

Results and discussion

Morphology and size distribution

The morphologies of all the samples were examined by SEM. Fig. 1 and Fig. 2 depicted the low-magnification and high-magnification SEM images.

When the content of Co^{2+} was fixed at 4 mmol, the morphology of the products changed distinctly with the content of NaOH. At a low NaOH content of 15 mmol, the as-synthesized particles were nearly mono-dispersed with spherical morphology (Sample 1). The average size of Sample 1 was about 2 μm (Fig. 1a and 2a). By increasing the NaOH content to 25 mmol, a perfect hexagonal morphology with sharp corners and edges could be found (Fig. 1b and 2b, Sample 2). These hexagons were about 1.4 μm in side-length and 25 nm in thickness (Fig. 2b). Interestingly, they always existed in the form of layered structure. Fig 2b clearly presented the state of the junction of adjacent hexagonal layers. At a higher content of NaOH (50 mmol), the uniform hexagonal shape was no longer apparent and these particles were consisted of many polyhedral structures (Fig. 1c and 2c, Sample 3).

For further investigating the effect of NaOH content on the products, the experiment concerning extra NaOH contents (10, 12.5 and 20 mmol) were designed. At the NaOH content of 10 and 12.5 mmol, the as-synthesized particles were solid spheres as Sample 1 (Fig. 3a-b). The surface of the products for 10 mmol NaOH was rough and became relatively smoother at higher NaOH content (Fig. 3a-c). By further increasing the NaOH content to 20 mmol, the particles began to exhibit hexagonal morphology. However, the surface for this kind of product was rough (Fig. 3d). Thus, through adjusting the ratio of Co^{2+}/NaOH (Co^{2+} content fixed with 4 mmol), the morphology of the products could be regulated from spherical to hexagonal shape. Meanwhile, it found that the surface roughness of product was also closely related with the ratio of Co^{2+}/NaOH.

For the sake of studying whether the same ratio of Co^{2+}/NaOH could result in the similar morphology, the morphologies of Sample 3 and Sample 4 were compared. The ratio of Co^{2+}/NaOH was 2/25 in both of them. However, the Co^{2+} and NaOH contents of Sample 3 were double those of Sample 4. Sample 3 was mainly composed of polyhedral structures as shown in Fig. 1c and 2c, partial of the particles exhibited irregular hexagonal shape. In contrast, Sample 4 was mainly consisted of spherical particles with size of 1 ~ 3 μm, only a few of the particles exhibited hexagonal-like shape (Fig. 1d and 2d, Sample 4). Thus, the morphology is the end product of both the contents and ratio of Co^{2+}/NaOH.

The morphologies of Sample 5 and 6 were illustrated Fig. 1e and 1f, which were found to consist of chain-like structures. The as-synthesized products of Sample 5 were long chains with some branches (Fig. 1e and 2e). The average diameter of chains was about 2 μm and lengths of the spherical chains were about 60 μm. Regarding Sample 6, in addition to sphere chain-like structure there could also find some small branches (Fig. 1f and 2f). The diameter of the sphere was about 1.5 μm. Moreover, it was tough to precisely determine the length of sphere chains, because parts of them attached together. Interestingly, the surfaces of the last two samples were composed of a number of nano-sheets, which could increase the surface areas of the chains (Fig. 2e and 2f).

Compared to Sample 3, the only changing parameter of Sample 5 was the lower Co^{2+} content. For Sample 1 and 6, they also possessed same ratio of Co^{2+}/NaOH, but the Co^{2+} content of Sample 6 was pretty low. It was considered that higher concentration of Co^{2+} would inhibit the diffusion and assemble of the particles while lower concentration would provide a good environment for these processes.[12] Thus, our results further suggesting that a lower concentration of Co^{2+} could favor the formation of chain structure.

Based on the above analysis, it was found that the contents and ratio of Co^{2+}/NaOH played a crucial role in the formation of products with different morphologies and sizes.

Structure characterization

XRD was used to confirm phase and crystal structure. Here, Sample 1, Sample 2 and

Sample 3 were chosen as representative samples for discussion (Fig. 4a, XRD results of other samples were shown in Fig. 4b). These samples had the same Co^{2+} content (4 mmol) with different NaOH contents (15, 25 and 50 mmol, respectively). All the XRD patterns, as shown in Fig. 4a, could be indexed with the pure cobalt. As known there are only two crystal structure for elemental cobalt, hexagonal-close-packed (hcp) and face-centered-cubic (fcc).[18] In Sample 1, diffraction peaks located at 2θ values of 44.5, 51.3 and 76.1° can be identified to the (111), (200) and (220) planes of fcc-cobalt (JCPDS 15-0806). The special (200) peak of fcc Co appeared in the pattern could distinguish the crystal structure from hcp Co at the position of 51.5°.[19] Sample 2 and 3 had mixed structures of both fcc-cobalt (JCPDS 15-0806) and hcp-cobalt (JCPDS 05-0727). Besides the same planes of fcc identified in Sample 1, (100), (002), (101) and (110) planes of hcp were also well indexed in Sample 2 and 3. The combination of fcc and hcp character was introduced by low activation energy for formation of stacking faults.[18, 20] Moreover, the proportion of hcp–cobalt increased with the increase of NaOH content, indicating that the cobalt was preferred to crystallize into hcp structure at higher alkali concentration. This result was coincident with the crystal structure of Co nanowires strongly depends on the pH.[19] The peak intensity was higher and the full width at half maximum (FWHM) was narrower, suggesting larger grain size and higher crystallinity of Sample 2.

XPS was applied to identify the electronic state and the composition using Sample 6 as representative. Three peaks locating at 284.8 eV, 531.2 eV and 781.0 eV were corresponded to the peaks of C1s, O1s and Co2p, respectively. Fig. 4c showed the Co 2p peaks. The XPS spectra presented two major peaks at 781.0 eV and 796.9 eV, corresponding to the Co $2p_{3/2}$ and Co $2p_{1/2}$ spin-orbit peaks of CoO. Note that two weak satellite peaks at 786.0 eV and 802.5 eV, about 5-6.8 eV higher than the positions of the two main peaks respectively, were clearly detected in the spectra, which is an important characteristic for the CoO phase.[21] This result was further accompanied by Raman spectra. Five Raman peaks were found and identified at 190, 468, 511, 608 and 672 cm^{-1} (Fig. 4d), corresponding to five Raman-active modes F_{2g}, E_g, F_{2g}, F_{2g}, and A_{1g}.[21, 22] The spectra confirmed the presence of oxidized cobalt in the form of CoO.

These above results suggested that the Co particles were covered with a thin layer of cobalt oxide protecting the material from oxidation in air and CoO is the main existence form of oxide on the surface of Co-core.

Growth mechanism

For a better understanding of the growth mechanisms, time-dependent experiments were carried out. The SEM images Fig. 5a showed the influences of different reaction times on the morphologies of Sample 1. In the early growth stage of 1 h, a number of tiny Co crystalline nuclei appeared and then the crystal growth followed. With the reaction time to 2 h, Co particles with an average size of 1 μm could be observed and the surface of these particles composed of numerous small nanoparticles, indicating the underdeveloped state. By further increasing the reaction time to 4.5 h, the dominant products were Co particles self-assembled into spheres with different sizes. And some of them aggregated together. At the end of the reaction (10 h), uniform Co spheres were formed (Fig. 1a and 2a). On the basis of the above results, the growth mechanism of solid spheres could be explained by Ostwald ripening process, in which crystal growth is in terms of larger particles at the expense of smaller particles.[23] For the formation of the chains, magnetic dipole-dipole interaction impelled the north and south poles of the dipolar particles attract each other into the assembly process.[14, 24] The assembly of small branches also caused by anisotropic magnetic forces.[25] Fig. 5b proposed the evolution of morphology of the Co spheres and chains on various growth stages.

The SEM images of Sample 2 at different stages were also observed (Fig. 5c). Single-layer and irregular hexagonal sheets were the dominating products in 1 h reaction. XRD result of Sample 2 (Fig. 4a) showed the (002) diffraction of hcp structure with a higher intensity, indicating that the crystallites were abundant in (001) facets and preferred to orient in the direction of [001]. Thus, longer reaction time leaded to three-dimensional self-assemblies in which the similar hexagonal particles arranged in the second layer along [001]. For this reason, Sample 2 exhibited hexagonal shapes and always existed in layered-structure. Meanwhile crystal growth in [110] brought about the increase in size. Fig. 5d illustrated the formation process of the hexagon.

Magnetic properties

According to the results of structure characterization, the as-synthesized products consisted of ferromagnetic Co nanoparticles embedded in an antiferromagnetic CoO. Furthermore, the magnetic properties of the as-synthesized samples at room temperature were measured. Hysteresis curves were shown in Fig. 6 and the inset presented a magnified hysteresis loops. All the samples exhibited hysteresis loops, indicating ferromagnetic behavior. Saturation magnetization *Ms*, remanent magnetization *M*r and coercivity *H*c were listed in Table 2. The highest *M*s presented in Sample 1 (162.5 emu/g) and Sample 6 (161.1 emu/g), a little lower than that of its bulk cobalt (168 emu/g).[26] Existence of impurities, antiferromagnetic CoO on surface and surface spin disorder would be responsible for the reduction of *M*s.[14] Antiferromagnetic CoO of the surface oxidation had been proved by XPS and Raman results, but it was hard to detect by XRD due to its minority (< 5%). Besides, the value of *M*s decreased with the increase of NaOH content. The coercivity *Hc* here were from 62 Oe to 104 Oe, which was much larger than that of bulk cobalt (10 Oe).[14, 26] The enhancement of *H*c maybe resulted from the small size, anisotropic shape and stacking faults.[10, 26] What was noteworthy was the coercivity of the as-synthesized Co microparticles were comparative to Co chains (90 Oe) but relatively lower than some nanostructures such as Co nanowires (166.8 Oe) and Co nanobelts (410.6 Oe), because the aspect ratio of our samples were lower than that of nanowires and nanobelts.[14, 17, 26]

Catalytic property

The catalytic behavior of the as-synthesized Co particles with different shapes on the thermal decomposition of AP was further investigated by TG-DSC.

For thermogravimetric analysis (TG) of pure AP, there was a weight loss below 75°C, which was attributed to dehydration of physical adsorbed water. The weight loss for thermal decomposition of pure AP contained two steps according to Fig 7a. The first step (17% weight loss) from 285.0°C to 340.0°C was attributed to the partial decomposition of AP to intermediate products such as NH_3 and $HClO_4$.[27] The second step (76% weight loss) from 340.0°C to 405.0° was caused by the complete decomposition to volatile gaseous products such as NO, O_2, Cl_2 and H_2O.[9] By adding 4% Co microparticles, the average initial and final thermal decomposition temperatures occurred at about 250.0°C and 320.0°C, indicating 4% Co microparticles made the decomposition temperature of AP decreased by 85°C. In the other words, the thermal decomposition rates of AP were accelerated as a result of adding Co microparticles.

For pure AP, the differential thermal analysis (DSC) curve revealed the thermal decomposition consisted of three stages. The first stage was an endothermic peak at about 244.3 °C (Fig 7b), which is due to the phase transition of AP from orthorhombic to cubic.[7-9, 28] The second and third stages were exothermic peaks appeared at about 318.5 °C and 393.5 °C respectively. At 318.5 °C, the small peak was ascribed to the partial decomposition of AP. At 393.5°C, the main exothermic peak, ascribed to the formation of a complete products. When 4 wt% catalysts were added to AP, there was no change in the position of endothermic peak, indicating Co microparticles had no effect on crystallographic transition temperature. However, the addition of Co microparticles made the second exothermic peak superpose to the first one, leading these two exothermic decomposition stages merged into one step. The exothermic peaks of Sample 1 to Sample 6 were 301.6, 314.1, 319.1, 313.8, 307.5 and 315.8°C respectively, which were 75-92°C lower compared to the complete decomposition temperature of pure AP. These results corresponded to the trend of TG measurements. The lower decomposition temperatures would bring higher the breakdown rate of propellants.

These data indicated that Co microparticles made AP quickly decomposed at lower temperatures and proved high catalytic activity in the AP-based propellant.

These TG-DSC data indicated the present catalytic activity of Sample 1 with spherical shapes was most active in all these samples with different morphologies. It is known that large specific surface areas could induce more reactive sites for catalyst.[29] Sample 1 was well mono-dispersed with narrow size distribution than other non-monodispersed samples (Fig. 1), indicating a relatively higher surface area and more surface reaction sites for catalytic activity.

Conclusions

Here, we report a facile route for the synthesis of Co sub-micro particles via one-step solvothermal method under ambient conditions and required no surfactants. By adjusting the content and ratio of Co^{2+}/NaOH, the sizes of the as-synthesized Co particles were varied from 1 μm to 3 μm while the morphologies including sphere, hexagon and chains were achieved. Meanwhile, three different growth mechanisms for these Co particles were proposed. The Co particles exhibited ferromagnetic behaviors. Furthermore, the Co particles had been found to possess good catalytic properties for the decomposition of ammonium perchlorate, especially the Sample 1 with narrow-sized nature of mono-disperse showed better catalytic activity than others and shifted the AP thermal decomposition temperature downwardly by about 93°C, which demonstrated its potential applications.

Acknowledgements

This work has been supported by the Beijing Natural Science Foundation (3142010) program, the Specialized Research Fund for the Doctoral Program of Higher Education of China (20130002110088) and Funding of State Key Lab of Tribology in Tsinghua University (SKLT2014A03).

Notes and references

1 V. F. Puntes, K. M. Krishnan and A. P. Alivisatos, *Science*, 2001, **291**, 2115-2117.
2 F. Dumestre, B. Chaudret, C. Amiens, M. C. Fromen, M. J. Casanove, P. Renaud and P. Zurcher, *Angew. Chem.-Int. Edit.*, 2002, **114**, 4462-4465.
3 Q. A. Pankhurst, J. Connolly, S. K. Jones and J. Dobson, *J. Phys. D-Appl. Phys.*, 2003, **36**, R167-R181.
4 Q. A. Pankhurst, N. T. K. Thanh, S. K. Jones and J. Dobson, *J. Phys. D-Appl. Phys.*, 2009, **42**, 224001.
5 S. Chaturvedi and P. N. Dave, *J. Saudi Chem. Soc.*, 2013, **17**, 135-149.
6 J. K. Sharma, P. Srivastava, S. Singh and G. Singh, *Energy Environ. Focus*, 2014, **3**, 121-130.
7 L. N. Jin, Q. Liu and W. Y. Sun, *Crystengcomm*, 2012, **14**, 7721-7726.
8 L. N. Jin, J. G. Wang, X. Y. Qian, D. Xia and M. D. Dong, *J. Nanomater.*, 2015.
9 H. Z. Duan, X. Y. Lin, G. P. Liu, L. Xu and F. S. Li, *Chin. J. Chem. Eng.*, 2008, **16**, 325-328.
10 S. L. Wen, Y. Liu, X. C. Zhao, J. W. Cheng and H. Li, *Phys. Chem. Chem. Phys.*, 2014, **16**, 18333-18340.
11 M. Liu, L. Chen, C. Lin, L. Zhang and H. Song, *J. Colloid Interface Sci.,* 2013, **410**, 116-123.
12 Z. T. Liu, X. Li, Z. W. Liu and J. Lu, *Powder Technol.*, 2009, **189**, 514-519.
13 R. N. Grass and W. J. Stark, *J. Mater. Chem.*, 2006, **16**, 1825-1830.
14 Y. J. Zhang, Q. Yao, Y. Zhang, T. Y. Cui, D. Li, W. Liu, W. Lawrence and Z. D. Zhang, *Cryst. Growth Des.*, 2008, **8**, 3206–3212.
15 J. S. Chen, T. Zhu, Q. H. Hu, J. Gao, F. Su, S. Z. Qiao and X. W. Lou, *ACS Appl. Mater. Interfaces*, 2010, **2**, 3628-3635.
16 H. Hilgendorff, B. Tesche and M. Giersig, *Aust. J. Chem.*, 2002, **54**, 497–501.
17 Q. Xie, Z. Dai, W. W. Huang, J. B. Liang, C. L. Jiang and Y. T. Qian, *Nanotechnology*, 2005, **16**, 2958-2962.
18 S. H. Sun and C. B. Murray, *J. Appl. Phys.*, 1999, **85**, 4325-4330.
19 F. S. Li, T. Wang, L. Y. Ren and J. R. Sun, *J. Phys.-Condes. Matter*, 2004, **16**, 8053-8060.
20 D. P. Dinega and M. G. Bawendi, *Angew. Chem.-Int. Edit.*, 1999, **38**, 1788-1791.

21 Q. Guan, J. L. Cheng, X. D. Li, B. Wang, L. Huang, F. D. Nie and W. Ni, *Sci Rep*, 2015, **5**.

22 S. H. Johnson, C. L. Johnson, S. J. May, S. Hirsch, M. W. Cole and J. E. Spanier, *J. Mater. Chem.*, 2010, **20**, 439-443.

23 W. Ostwald, *Z. Phys. Chemie-Stoch Ve*, 1900, **34**, 495-503.

24 V. Salgueiriño-Maceira, M. A. Correa-Duarte, A. Hucht and M. Farle, *J. Magn. Magn. Mater.*, 2006, **303**, 163-166.

25 N. Vandewalle and M. Ausloos, *Phys. Rev. E*, 1997, **55**, 94-98.

26 B. Q. Xie, Y. T. Qian, S. Y. Zhang, S. Q. Fu and W. C. Yu, *Eur. J. Inorg. Chem.*, 2006, 2454-2459.

27 M. Zou, X. H. Jiang, L. D. Lu and X. Wang, *J. Hazard. Mater.*, 2012, **225-226**, 124-130.

28 S. S. Lu, X. Y. Jing, J. Y. Liu, J. Wang, Q. Liu, Y. H. Zhao, S. Jamil, M. L. Zhang and L. H. Liu, *J. Solid State Chem.*, 2013, **197**, 345-351.

29 X. J. Shen, J. P. Yang, Y. Liu, Y. S. Luo and S. Y. Fu, *New J. Chem.*, 2011, **35**, 1403-1409.

Table 1 Synthesis conditions for the preparation of typical samples

Sample No.	$CoCl_2.6H_2O$ [mmol]	NaOH [mmol]
1	4	15
2	4	25
3	4	50
4	2	25
5	2	50
6	1	15

Table 2 Magnetic properties of the as-synthesized products

Sample No.	1	2	3	4	5	6
*M*s [emu/g]	162.5	158.5	149.1	140.4	134.3	161.1
*M*r [emu/g]	6.51	7.61	9.63	5.62	7.79	10.38
*H*c [Oe]	74.76	80.22	104.30	62.24	97.28	90.08

Figure Captions

Fig. 1 Low-magnification SEM images of the Co as-synthesized samples: (a) Sample 1, (b) Sample 2, (c) Sample 3, (d) Sample 4, (e) Sample 5, (f) Sample 6.

Fig. 2 High-magnification SEM images of the Co as-synthesized samples: (a) Sample 1, (b) Sample 2, (c) Sample 3, (d) Sample 3, (e) Sample 5, (f) Sample 6. The insets show the TEM images of Sample 1 and Sample 2.

Fig. 3 SEM images of Co products synthesized under 4 mmol Co^{2+} with different NaOH contents: (a) 10 mmol, (b) 12.5 mmol, (c) 15 mmol, (d) 20 mmol.

Fig. 4 Structure characterization of Co as-synthesized samples. (a) XRD patterns of typical Samples 1-3, (b) XRD patterns of typical Samples 4-6, (c) XPS spectra of Sample 6, (d) Raman spectra of Samples 1-6.

Fig. 5 Growth mechanism of the Co as-synthesized samples. (a) SEM images of the sample 1 at different reaction stage, (b) Schematic illustration of the Sample 1 and 6, (c) SEM images of the Sample 2 at different reaction stage, (d) Schematic illustration of the Sample 2.

Fig. 6 Magnetization hysteresis loops of the Co as-synthesized samples at room temperature. The inset shows magnified hysteresis loops from -450 to 450 Oe.

Fig. 7 Catalytic performance of Co as-synthesized samples on the thermal decomposition of ammonium perchlorate (AP). (a) DSC curves of mixtures of AP and Co samples; (b) TG curves of mixtures of AP and Co samples.

Figure 1

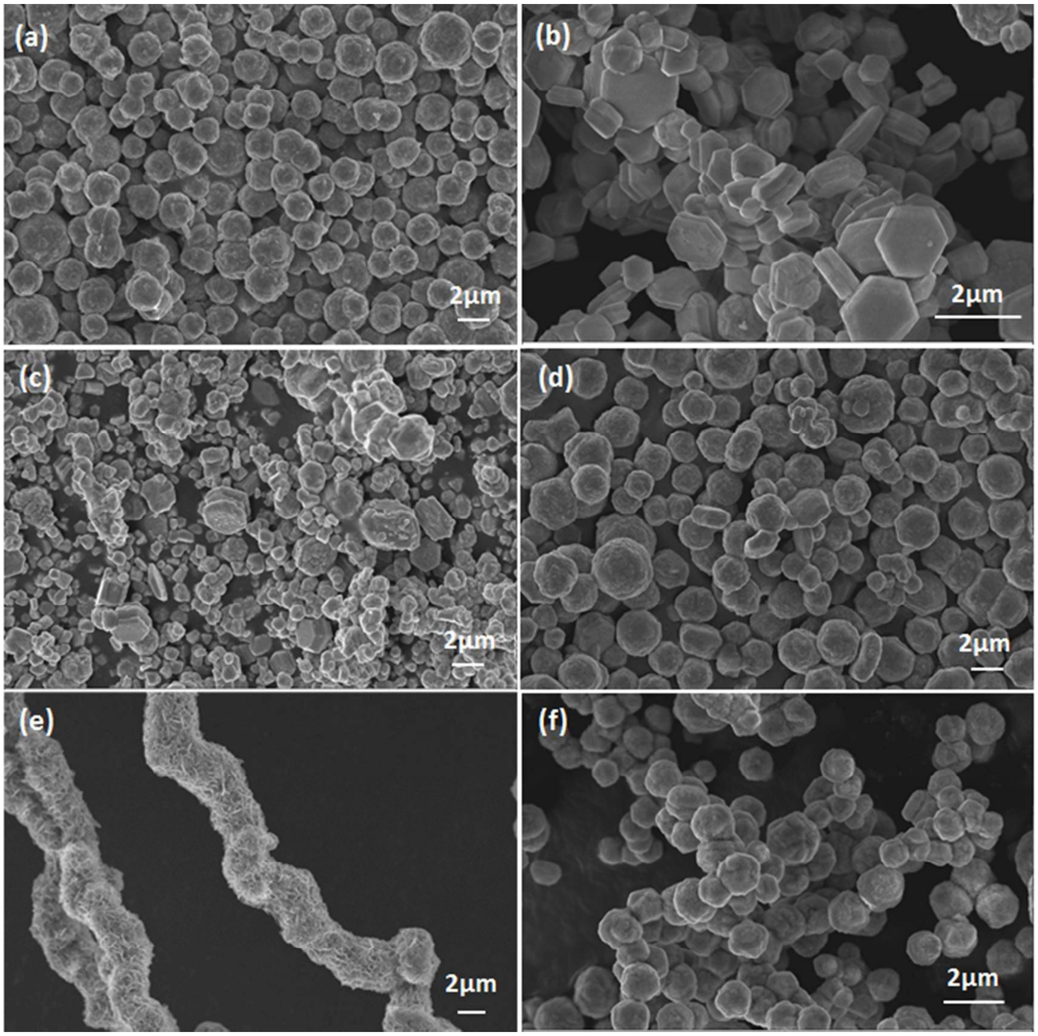

Figure 2

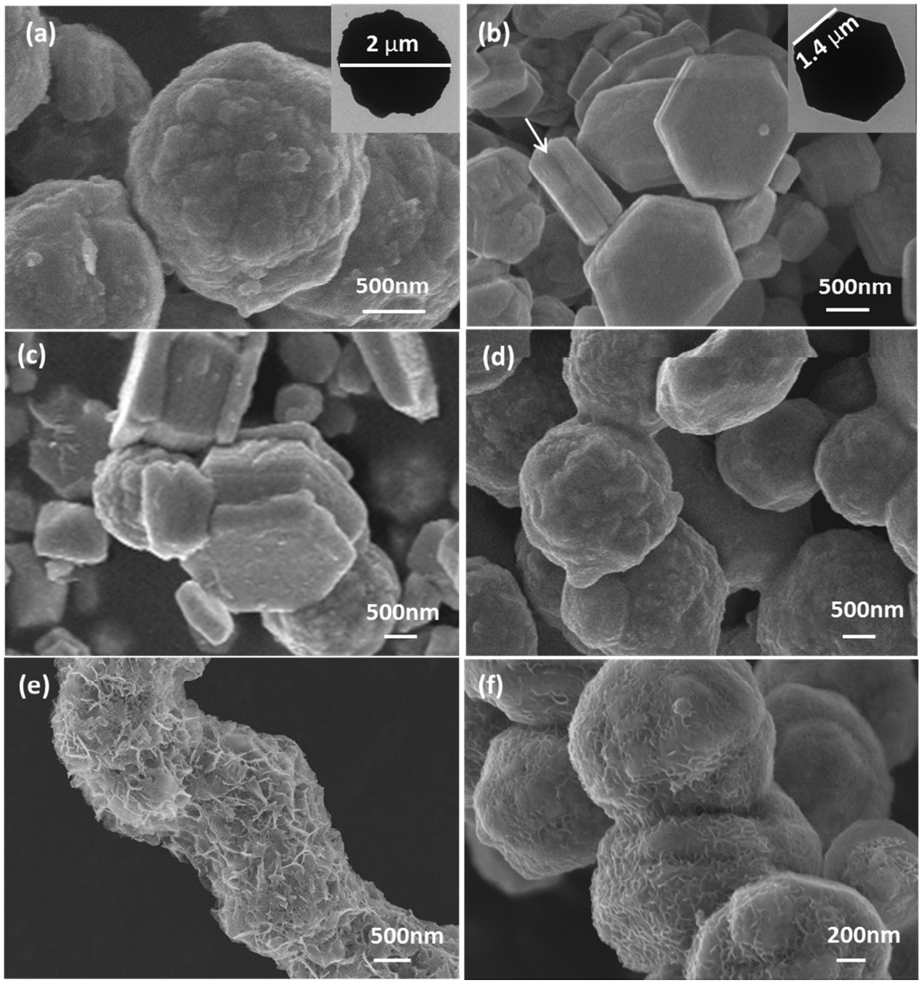

Figure 3

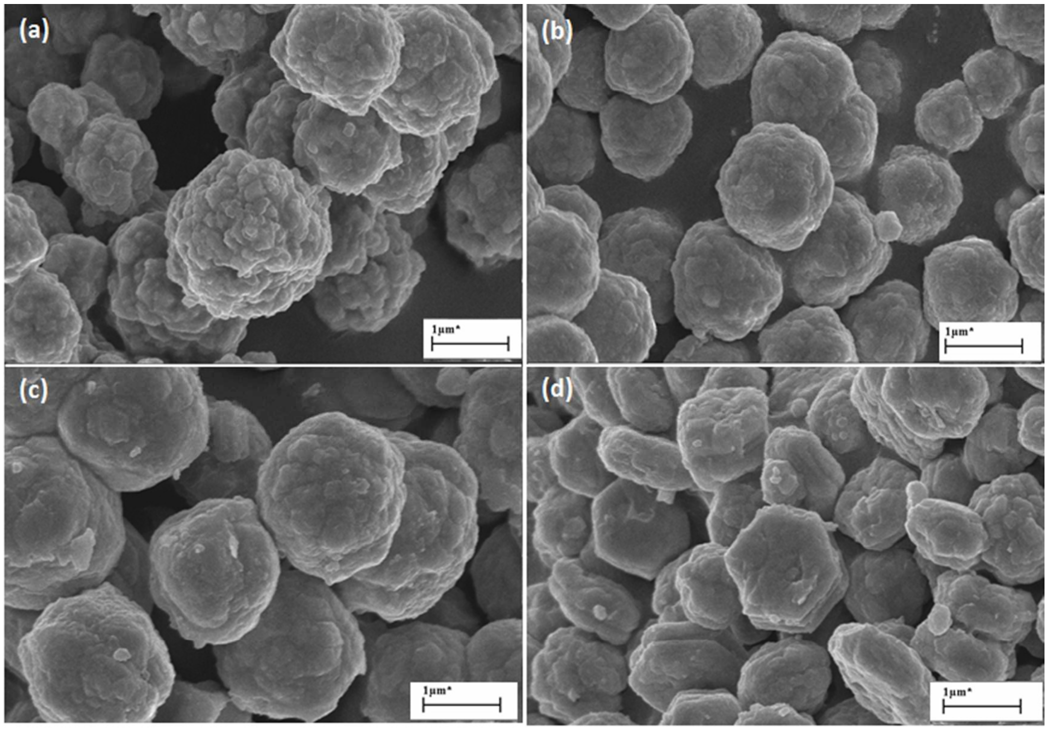

Figure 4

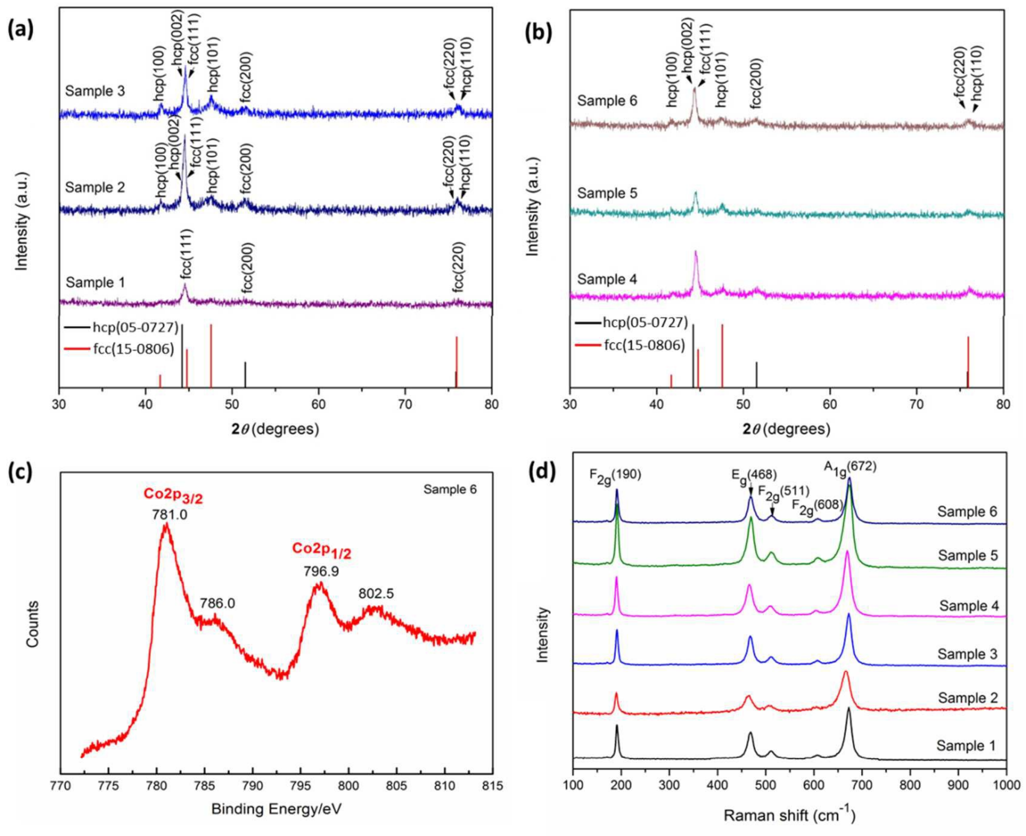
(a)
Sample 3
Sample 2
Sample 1
hcp(100)
hcp(002)
fcc(111)
hcp(101)
fcc(200)
fcc(220)
hcp(110)
hcp(05-0727)
fcc(15-0806)
Intensity (a.u.)
2θ (degrees)
(b)
Sample 6
Sample 5
Sample 4
(c)
Sample 6
Co2p3/2
781.0
786.0
Co2p1/2
796.9
802.5
Counts
Binding Energy/eV
(d)
F2g(190)
Eg(468)
F2g(511)
F2g(608)
A1g(672)
Intensity
Raman shift (cm-1)

Figure 5

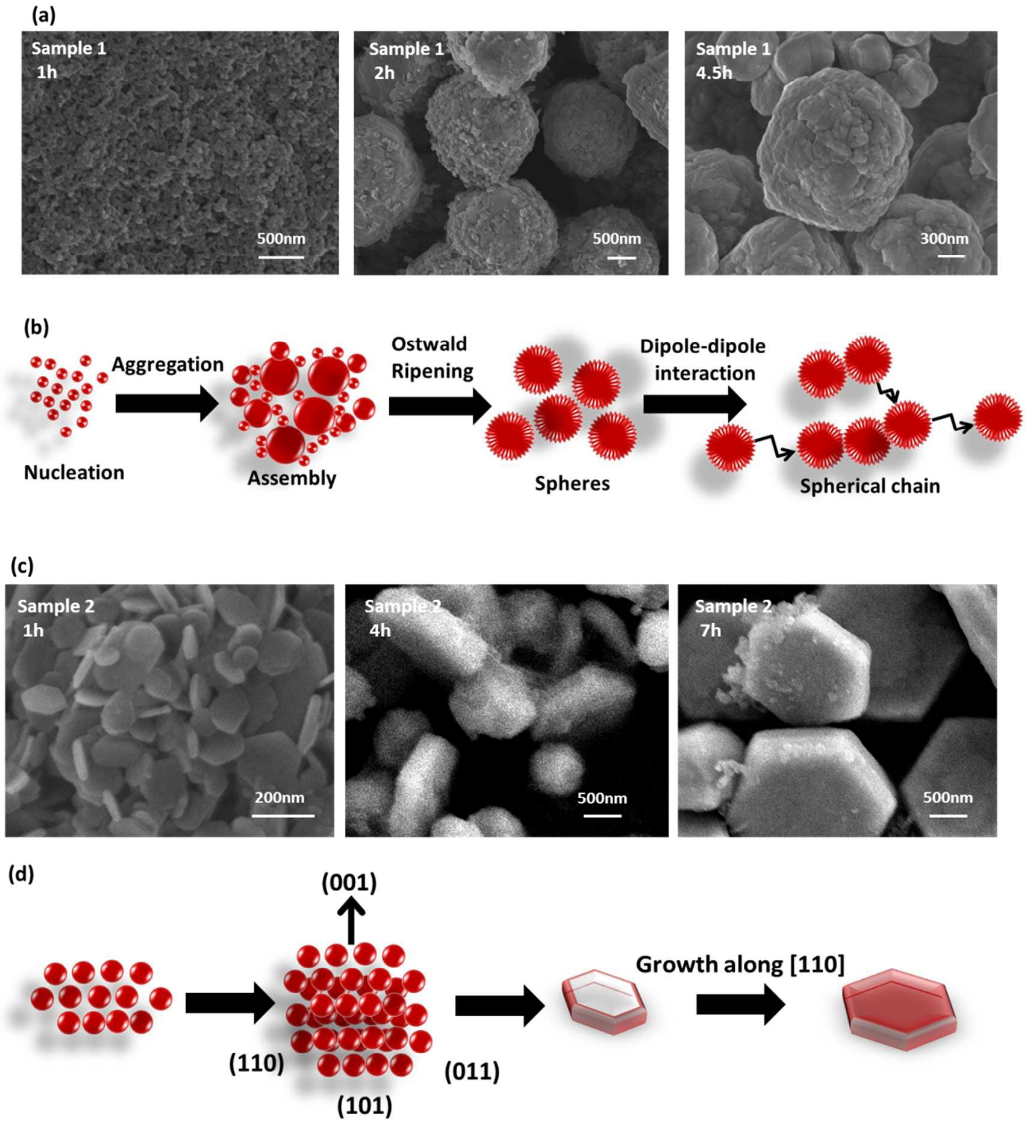
(a)
Sample 1 1h
500nm
Sample 1 2h
500nm
Sample 1 4.5h
300nm
(b)
Aggregation
Ostwald Ripening
Dipole-dipole interaction
Nucleation
Assembly
Spheres
Spherical chain
(c)
Sample 2 1h
200nm
Sample 2 4h
500nm
Sample 2 7h
500nm
(d)
(001)
Growth along [110]
(110)
(011)
(101)

Figure 6

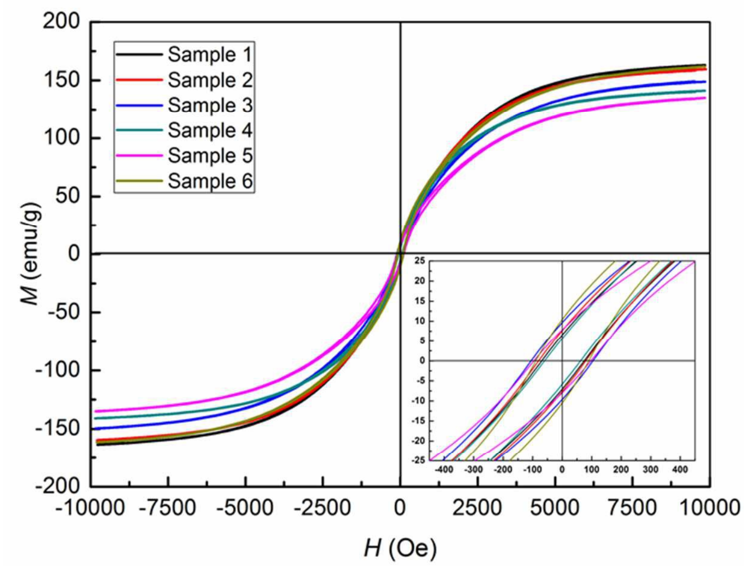
Sample 1
Sample 2
Sample 3
Sample 4
Sample 5
Sample 6
M (emu/g)
H (Oe)

Figure 7

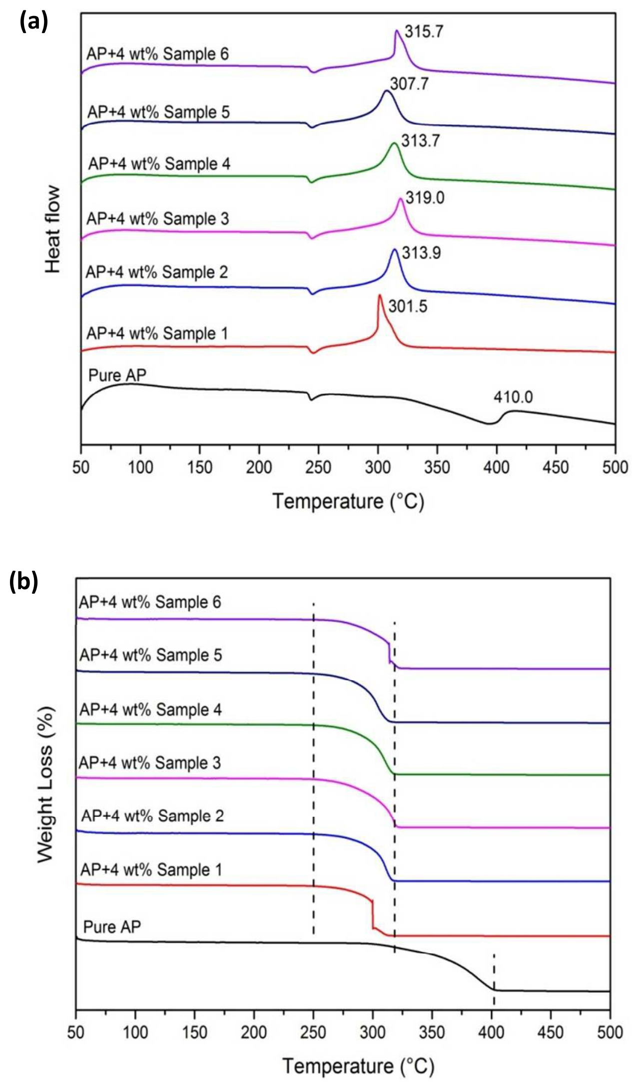
(a)
AP+4 wt% Sample 6
315.7
AP+4 wt% Sample 5
307.7
AP+4 wt% Sample 4
313.7
AP+4 wt% Sample 3
319.0
AP+4 wt% Sample 2
313.9
AP+4 wt% Sample 1
301.5
Pure AP
410.0
Heat flow
50 100 150 200 250 300 350 400 450 500
Temperature (°C)
(b)
AP+4 wt% Sample 6
AP+4 wt% Sample 5
AP+4 wt% Sample 4
AP+4 wt% Sample 3
AP+4 wt% Sample 2
AP+4 wt% Sample 1
Pure AP
Weight Loss (%)
50 100 150 200 250 300 350 400 450 500
Temperature (°C)